

Topological Fluid Dynamics: Theory and Applications

Evolution of the leading-edge vortex over an accelerating rotating wing

Yossef Elimelech^{a*}, Dmitry Kolomenskiy^b, Stuart B. Dalziel^c, H. K. Moffatt^c

^a*Faculty of Aerospace Engineering, Technion-Israel Institute of Technology, Haifa 32000, Israel*

^b*Centre Européen de Recherche et de Formation Avancée en Calcul Scientifique, 42 avenue Gaspard Coriolis, 31057 Toulouse Cedex 01, France*

^c*Department of Applied Mathematics and Theoretical Physics, Centre for Mathematical Sciences, University of Cambridge, Wilberforce Road, Cambridge CB3 0WA, United Kingdom*

Abstract

The flow field over an accelerating rotating wing model at Reynolds numbers Re ranging from 250 to 2000 is investigated using particle image velocimetry, and compared with the flow obtained by three-dimensional time-dependent Navier-Stokes simulations. It is shown that the coherent leading-edge vortex that characterises the flow field at $Re \sim 200$ -300 transforms to a laminar separation bubble as Re is increased. It is further shown that the ratio of the instantaneous circulation of the leading-edge vortex in the acceleration phase to that over a wing rotating steadily at the same Re decreases monotonically with increasing Re . We conclude that the traditional approach based on steady wing rotation is inadequate for the prediction of the aerodynamic performance of flapping wings at Re above about 1000.

© 2013 The Authors. Published by Elsevier B.V.

Selection and/or peer-review under responsibility of the Isaac Newton Institute for Mathematical Sciences, University of Cambridge

Keywords: flapping flight; unsteady aerodynamics; leading-edge vortex evolution; particle image velocimetry; Navier-Stokes simulations

* Corresponding author

E-mail address: yosie@aerodyne.technion.ac.il

Nomenclature

\bar{c}	mid-span chord length
R	wing span
X	dimensional coordinate in the streamwise direction (wing frame of reference)
Y	dimensional coordinate parallel to the axis of rotation
Z	dimensional spanwise coordinate in the wing frame of reference
x	dimensionless coordinate in the streamwise direction (wing frame of reference), $x = X/\bar{c}$
y	dimensionless coordinate parallel to the axis of rotation, $y = Y/\bar{c}$
z	dimensionless spanwise coordinate in the wing frame of reference, $z = Z/R$
t	time from start of stroke motion
τ	time constant
\mathbf{U}	dimensional flow velocity components in the wing frame of reference
\mathbf{u}	dimensionless flow velocity components in the wing frame of reference, $\mathbf{u} = \mathbf{U}/(zR\dot{\theta})$
u_z	dimensionless spanwise velocity component
θ	angular location from start of stroke motion
$\dot{\theta}_\infty$	angular velocity of wing in steady rotation
α	geometric angle-of-attack
ν	fluid kinematic viscosity
Re	Reynolds number, $\text{Re} = \dot{\theta}_\infty R \bar{c} / \nu$
ω_z	dimensional spanwise vorticity
$\hat{\omega}_z$	dimensionless spanwise vorticity, $\hat{\omega}_z = \omega_z \bar{c} / (zR\dot{\theta})$
Γ	circulation
Σ	symmetric part of velocity gradient tensor
Ω	antisymmetric part of velocity gradient tensor

1. Introduction

Flapping flight has been a subject of interest for several centuries since the visionary ideas of Roger Bacon and Leonardo da Vinci. Since Weis-Fogh's [1] analysis of hovering animal flight, many authors have studied flow mechanisms of hovering insects, and our understanding of insect flight mechanisms has advanced significantly over the last two decades through many experimental and numerical explorations. Most studies fall into two main groups: the first analyses the flow over periodically flapping wings; the second analyses the flow over rotating wings like propellers, simulating the mid-stroke of the flapping cycle but not the wing rotation at the end of each cycle.

For insects, it is generally accepted that most of the lift is associated with a large, stable leading-edge vortex (LEV) which separates from the sharp leading edge of the wing [2]. Other features of this leading-edge vortex, such as its spanwise distribution [3, 4] or its stability [5, 6], are more controversial. Usherwood & Ellington [7] showed that the LEV is stable on a steadily rotating wing like a propeller. The resultant aerodynamic force is normal to the wing surface, reflecting the fact that the LEV essentially eliminates the leading-edge suction. The practical consequence of this result is a low lift-to-drag ratio; the high vertical force coefficients measured in propeller tests for various aspect ratios and Reynolds numbers Re were therefore inevitably associated with high aerodynamic drag.

An important aspect of hovering flight which cannot be treated using steadily rotating wings is the lift evolution after the abrupt wing rotation (about the wing axis) which occurs at either end of the wing stroke. During each end-of-stroke rotation, the existing LEV separates from the wing surface and a 'newly born' LEV is formed once the wing starts to accelerate through the following wing stroke. It is important to determine the time-scale of development of the new LEV as this is directly related to the time it takes for the aerodynamic lift (and drag) to reach its ultimate value. While optimistic estimates assume immediate formation of the LEV, more realistic evaluations are needed to better understand the detailed flow mechanisms of hovering flight.

A recent study [8] discussed the time evolution of the flow field over a dynamically-scaled flapping wing at $\text{Re} =$

250 and angle-of-attack $\alpha = 50^\circ$. It is believed that such a high angle-of-attack is unlikely to be representative of insect flight; we therefore initiated the present study with an experiment at $Re = 250$ and $\alpha = 30^\circ$.

Micro air vehicles are currently designed for Reynolds numbers that are higher than this by an order of magnitude or more, yet little is known about the nature of the transient flow field over flapping wings in this regime. The present experimental study discusses the evolution of the flow field and the formation of the leading-edge vortex over an accelerating rotating wing up to $Re = 2000$. We observed a coherent LEV at $Re = 250$; a separation bubble bounded by a sheet of vorticity shed from the leading edge at $Re = 1000$; and an instability of this vortex sheet at $Re = 2000$. We focus on the first quarter of the wing flapping cycle, i.e. half of the stroke of a flapping wing. The flow field during this acceleration phase is compared to the flow that develops over a steadily rotating wing in order to highlight the differences between the two. We find that at the end of the first quarter of a cycle, the circulation around the wing exceeds its steady-state value at $Re = 250$, but that at $Re = 1000$ it remains below the corresponding steady-state value. Later, we discuss the question, important for engineering applications, as to whether the flapping-wing strategy is aerodynamically advantageous at Reynolds numbers above 250 as compared with steady wing rotation.

2. Setup and methods

2.1. Experimental setup

The study was performed using a controlled wing suspended in a Perspex tank ($400 \times 400 \times 500$ mm) filled with water-glycerin solution of kinematic viscosity $\nu = 3.92 \cdot 10^{-6} (\pm 6\%)$ m²/s (Fig. 1a and c). A real-time control unit (National Instruments cRIO-9022 controller together with the NI-9505 DC brushed servo module) controlled a servo motor which rotated the wing around a vertical axis. The wing's planform was a triangle machined from a 1.5 mm thick stainless steel flat plate. The distance between the centre of rotation and the wing tip (i.e. the wing length) was $R=100$ mm and the tip chord length was 50 mm (Fig. 1b).

The flow field was obtained using two-dimensional particle image velocimetry. Data was acquired at five equidistant span locations between $Z/R = 0.4$ and $Z/R = 0.8$ (see Fig. 1b), where Z is the coordinate along the span. Using a high frame-rate digital camera (Photron FASTCAM-ultima APX 120K, 1000 by 1000 pixel resolution) and a Nikon 60 mm f/2.8G ED AF-S Micro NIKKOR lens, a field of view of approximately 60 by 60 mm was recorded. This allowed capturing the flow over the entire chord at all span locations and some of the flow details of the near wake. Silver-coated hollowed glass spheres with a mean diameter of 10 μ m (Dantec Dynamics Ltd.) were used as seeding particles. The flow was illuminated by a high repetition dual cavity Nd:YLF laser head (10 mJ/pulse per cavity at 527 nm). A cylindrical lens ($f = 7.8$ mm) was used to create a thin light sheet approximately 2 mm thick; the light sheet illuminated several span stations, as shown in Fig. 1b.

During the wing motion, high frame-rate image sequences were recorded at several angular wing positions, namely, $\theta=10, 22.5, 45, 67.5$ and 90° , from the start of the motion. Using information from the servo motor encoder, a synchronisation pulse was fired to the camera and the laser head at these specific angular locations. In order to keep the same camera calibration and illumination settings, the initial angular position of the wing was modified to allow image capturing at a fixed location with respect to the camera. For better signal-to-noise ratio, each case was repeated 20 times. At the end of each wing stroke the wing decelerated to rest, and a pause of approximately 60s was inserted between two successive wing strokes to establish an essentially quiescent flow at the beginning of each stroke. The PIV processing was conducted using DigiFlow [9]. For each PIV plane, two in-plane velocity components were computed from the cross-correlation of pairs of successive images with 50% overlap between the interrogation domains. The high seeding density allowed high quality vector fields for interrogation windows of 21 by 21 pixels.

2.2. Numerical setup

Rigid wings moving in an incompressible viscous fluid are considered, as described in [10]. The no-slip boundary condition at the solid boundary is modelled using the volume penalisation method [11]. The penalised Navier-Stokes equations are solved using a classical Fourier pseudo-spectral method. The spatial computational domain is a rectangular box with periodic boundary conditions imposed on all its faces. The computational domain of size $L_x \times L_y \times L_z = 12^3$ was uniformly discretised with 768^3 grid points. The time integration is exact for the viscous term and

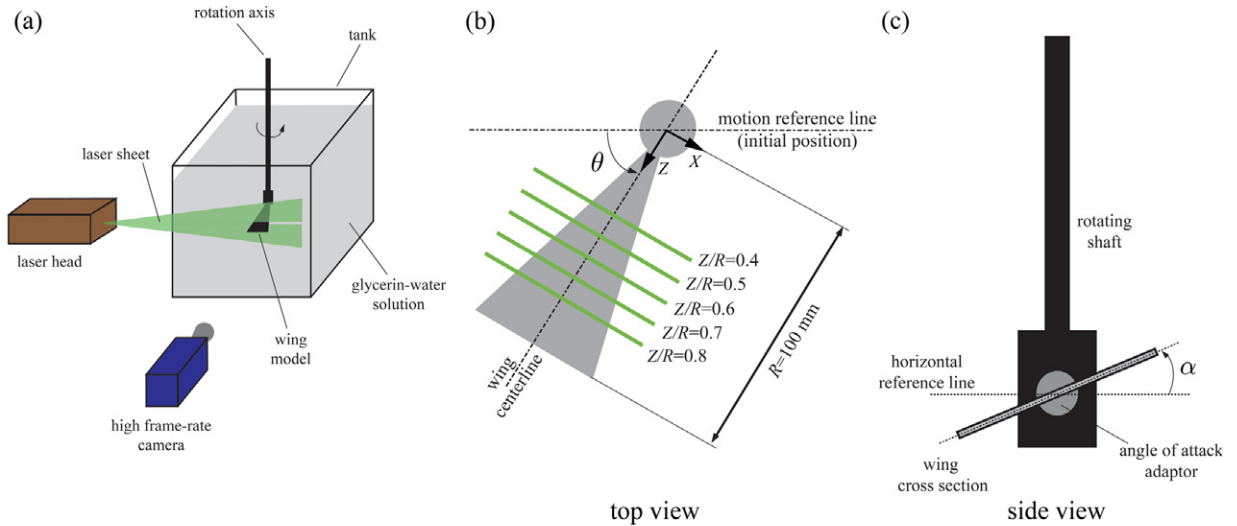


Fig. 1. Experimental setup: (a) general illustration showing the tank, the rotating wing and the camera-illumination setup; (b) top view of the wing-shaft assembly showing the wing planform, the rotation angle and the planes where images were obtained; (c) side view of the wing-shaft assembly showing the geometric angle-of-attack with respect to the horizon.

an adaptive second-order Adams-Bashforth scheme is used for the nonlinear term [12]. The parallel implementation of the code employs the P3DFFT fast Fourier transform package.

2.3. Kinematics

In order to parameterise the complex motion of a flapping wing, the wing kinematics was simplified to an angular motion at a constant geometric angle-of-attack of 30° (Fig. 1c). Starting from rest, the wing followed the kinematic relation $\dot{\theta}/\dot{\theta}_\infty = (1 - e^{-t/\tau})$, where θ is the wing rotation angle, $\dot{\theta}_\infty$ is the ultimate angular velocity of the wing, t is elapsed time from motion start and τ is a time constant. In order to represent a realistic manoeuvre of a periodically flapping wing, the motion was subject to the kinematical constraints $\dot{\theta}/\dot{\theta}_\infty(t^*) = 0.99$, $\theta(t^*) = \pi/2$. The Reynolds number $Re = \dot{\theta}_\infty R \bar{c} / \nu$ is based on the maximal tip velocity $\dot{\theta}_\infty R$, the mid-span chord of the wing $\bar{c} = R/4$, and the kinematic viscosity ν ; in this study, Re ranged from 250 to 2000.

2.4. Flow diagnostics

In order to establish a comparison of the flow field over the wing, the velocity field \mathbf{U} , and the spanwise vorticity component ω_z , were referenced to the wing's instantaneous circumferential velocity at each span. In particular, the dimensionless velocity components and the spanwise vorticity fields are $\mathbf{u} = \{u_x, u_y, u_z\} = \mathbf{U}/(zR\dot{\theta})$ and $\hat{\omega}_z = \omega_z \bar{c}/(zR\dot{\theta})$, respectively, where Z is the radial position, R the wing length, \bar{c} the mid-span chord and $z = Z/R$ the dimensionless radial location; using this terminology, the dimensionless spanwise velocity component is denoted by u_z (positive towards the wing tip). Whenever the velocity vector field is shown below, it is given in the wing frame of reference, not in the inertial frame.

The LEV region was identified using the dimensionless second invariant of the velocity gradient tensor [13]:

$$E = (\|\Sigma\|^2 - \|\Omega\|^2) / (\|\Sigma\|^2 + \|\Omega\|^2), \quad (1)$$

where Σ and Ω are the symmetric and antisymmetric components of the velocity gradient tensor:

$$\Sigma = \frac{1}{2}(\nabla \mathbf{u} + (\nabla \mathbf{u})^T), \quad \Omega = \frac{1}{2}(\nabla \mathbf{u} - (\nabla \mathbf{u})^T). \quad (2)$$

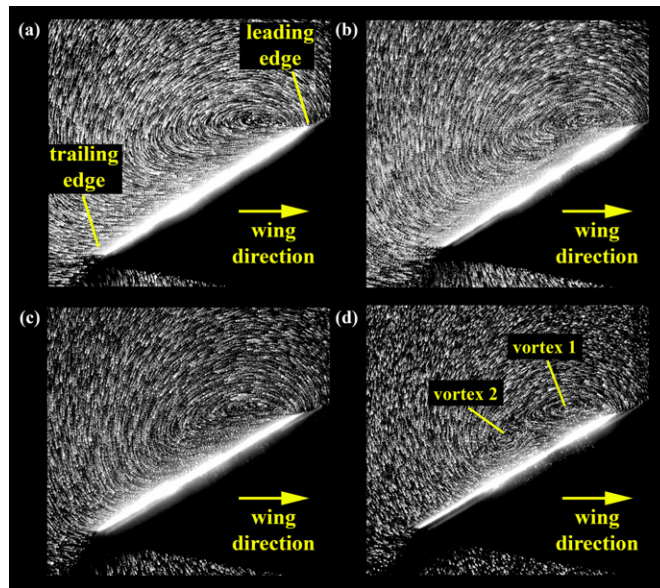


Fig. 2. Streaklines, as a function of Reynolds number, generated from the high-speed video recordings at $z = 0.6$, $\theta = 67.5^\circ$. (a) $Re = 250$ (b) $Re = 500$ (c) $Re = 1000$ (d) $Re = 2000$.

By its definition, this measure E satisfies $|E| < 1$; the value $E = -1$ represents vortical flow, while the values 0 and +1 represent shearing and irrotational flows, respectively. In this study, the LEV region was identified as the region where $E < 0$ and $\hat{\omega}_z > 0$; this specification provided an objective measure and was found to be less sensitive than conventional techniques based on an arbitrary vorticity threshold. The circulation within the LEV was calculated by integrating $\hat{\omega}_z$ over the LEV region, thus defined.

3. Results and discussion

Figure 2 shows synthesised streak images generated by overlaying high-speed video images. These images provide a qualitative description of the evolution of the LEV at $z = 0.6$ and $\theta = 67.5^\circ$. The LEV is represented by the counter-clockwise spanwise vorticity concentration (Fig. 3); at $Re = 250$ the LEV was large in size (Fig. 2a) and remained stable throughout the acceleration phase and thereafter during the steady wing rotation, although it was somewhat detached from the wing surface. At higher Re , the size of the LEV decreased monotonically (Fig. 2b, c) and remained fixed (stable) to the wing's leading edge. The topology of the LEV changed at Reynolds number 2000; instead of the single vortex that characterized the flow field at the lower Reynolds numbers, at $Re = 2000$ the vortex was split into two separate vortices (vortex 1 and vortex 2 in Fig. 2d). The present study focuses on the development of the LEV only when circumstances are such that its ultimate state during steady rotation is stable; we therefore restrict attention here to Reynolds numbers below 2000. (The question of LEV stability will be treated in a later publication.)

Quantitative measurements (see Fig. 3) describe the flow field evolution during the acceleration phase at $Re = 250$ and 1000. At $Re = 250$, shortly after the start of the motion (at $\theta = 10^\circ$) the LEV was concentrated in the vicinity of the leading-edge (Fig. 3a) and developed to its ultimate size as the wing approached $\theta = 45^\circ$ (Fig. 3b, c). During this time a boundary layer along the pressure side of the wing developed; thanks to the low Reynolds number the starting vortex was somewhat diffused (see Fig. 3a) in the vicinity of the trailing-edge. At $Re = 1000$, the highest Reynolds number at which a stable LEV was obtained, the vorticity was spread over more of the wing; from this fact we describe the flow structure that evolved over the suction side of the wing as a *separation-bubble* rather than as a *leading-edge vortex* (which characterises the flow when $Re \sim 10^2$). At $Re = 1000$, the vorticity developed monotonically during the acceleration phase and did not reach a steady-state during the first 90° of the wing motion. Furthermore, while at $Re = 250$ the highest $\hat{\omega}_z$ value was measured in the vicinity of the leading-edge, the maximal $\hat{\omega}_z$ value at $Re = 1000$

(Fig. 3e, f) was measured in the vicinity of the flow reattachment point. This intense vorticity encouraged induced reversed velocity which, in turn, created a 'dead-water' zone inside the separation-bubble; this zone is characterized by low $\hat{\omega}_z$ values near the wing surface and a shear layer above it.

Good agreement between the experimental and numerical results (see representative example in Fig. 4) allowed us to use the latter to obtain the spanwise velocity component u_z , which could not be resolved experimentally using two-dimensional particle image velocimetry. This spanwise component provides a clear distinction between the flow field over a rotating wing, and that over a wing in rectilinear motion. A rotating wing experiences a non-uniform spanwise pressure distribution due to the linearly varying circumferential velocity at each radial location along the wing span. In such circumstances, the flow field is fully three-dimensional, especially near the root of the wing [6, 14]¹. This phenomenon has already been found to yield high cross-sectional lift coefficients [14]; other studies associated the augmented lift capacity and postponed stall characteristics with the stability of the LEV which is itself correlated with u_z [6]. In these scenarios, the LEV was found to remain attached along the median portion of the wing while further out toward the wing tip the LEV lost its coherence and experienced vortex breakdown. As mentioned earlier, we restrict attention in the present discussion to cases where the LEV was found to remain attached to the wing surface.

We attempted to correlate between the evolution of the spanwise flow and the spanwise vorticity production because the latter is a direct measure of the aerodynamic load acting on the wing. The evolution of u_z during the acceleration phase is shown in Fig. 5 for $Re = 250$. As expected, u_z increased immediately after the motion began (Fig. 5a). At $z = 0.4$ and $\theta = 10^\circ$, u_z reached approximately 0.2. Later, when the wing approached $\theta = 90^\circ$ (mid-stroke) u_z attained a value as high as 1.2, exceeding the wing's instantaneous circumferential velocity at that spanwise station (emphasising the three-dimensional character of the flow). Not only did u_z evolve during the acceleration phase, it was also non-uniformly distributed along the wing span, as shown in Fig. 6 for $Re = 500$ at $\theta = 90^\circ$. The highest u_z was measured near the wing root (Fig. 6a), and it decayed monotonically along the span towards the wing tip (Fig. 6c). Interestingly, u_z was not confined to the region where $\hat{\omega}_z$ was maximal (i.e. within the LEV region); this phenomenon is at variance with earlier discussions which have associated the stability of an LEV solely with the presence of high spanwise flow within the LEV core; in a case where the LEV stability was solely u_z dependent, higher values of u_z should have been associated with an attached LEV. In turn, the current results at $Re = 2000$ showed a non-stationary dual-core LEV (Fig. 2d) while u_z peaked to its highest value at that Reynolds number. Therefore, we suggest that the fluid viscosity (which of course affects the local Reynolds number at each span location) is another key factor which may inhibit the growth-rate of possible flow disturbances and preserve the LEV coherence.

In order to describe the role of the spanwise flow, we show its correlation with the vorticity production within the LEV. To this end, $\hat{\omega}_z$ within the LEV was integrated during the acceleration phase and thereafter during the steady rotation, yielding the LEV circulation; its evolution is described below as the ratio between the instantaneous circulation and that obtained during steady wing rotation, $\Gamma_{LEV}/\Gamma_{LEV,\infty}$. $\Gamma_{LEV,\infty}$ was calculated from flow measurements acquired following five successive periods of steady wing rotation. The evolution of the LEV circulation is presented in Fig. 7 for three different Reynolds numbers. The initially high circulation growth rate is explained by the fact that the spanwise velocity component was small at the initial stage of the wing motion (Fig. 5a). The low spanwise velocity induced low vorticity convection towards the tip and encouraged vorticity accumulation. Only later, when the spanwise velocity component grew considerably, did the growth rate of Γ_{LEV} decay following the same mechanism.

The evolution of u_z also explains the differences in the LEV circulation growth along the span: at the middle of the stroke Γ_{LEV} approached approximately its steady-state value at the most distal span station, $z = 0.8$, (Fig. 7) while at the most medial span station ($z = 0.4$) Γ_{LEV} reached only 80 percent of its ultimate steady-state value at the same instant.

Interestingly, at the lowest end of the Reynolds number range ($Re = 250$), the circulation evolution during the acceleration phase showed some aerodynamic benefits since the circulation attained a level which exceeded its asymptotic steady wing rotation value. The results clearly show that $\Gamma_{LEV}/\Gamma_{LEV,\infty}$ decreases as Reynolds number increases (Fig. 7); we believe that two effects contribute to this phenomenon: first, the separation-bubble region is considerably longer at larger Reynolds numbers; a longer time is therefore needed to convect vorticity in the chord direction.

¹The flow field is also fully three-dimensional near the wing tips; however, this feature is generally present in the flow over a translating finite wing as well as in that over a rotating finite wing.

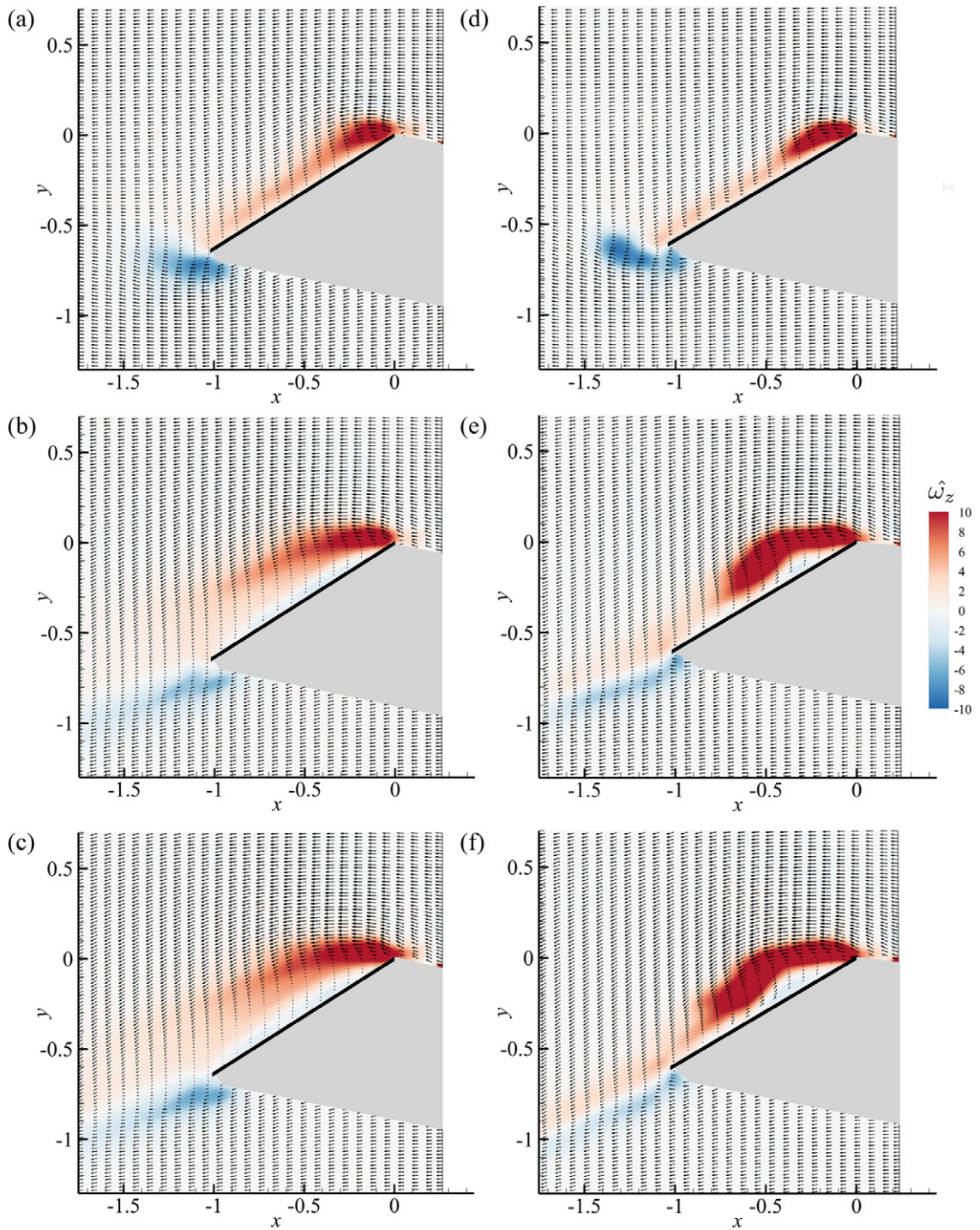


Fig. 3. Flow field evolution at $Re = 250$ (left panels) and $Re = 1000$ (right panels), $z=0.6$, during the wing acceleration, showing contours of $\hat{\omega}_z$. (a,d) $\theta = 10^\circ$; (b,e) $\theta = 45^\circ$; (c,f) $\theta = 90^\circ$. For clarity, only representative velocity vectors are shown. Gray shading indicates the light-sheet-shadow regions.

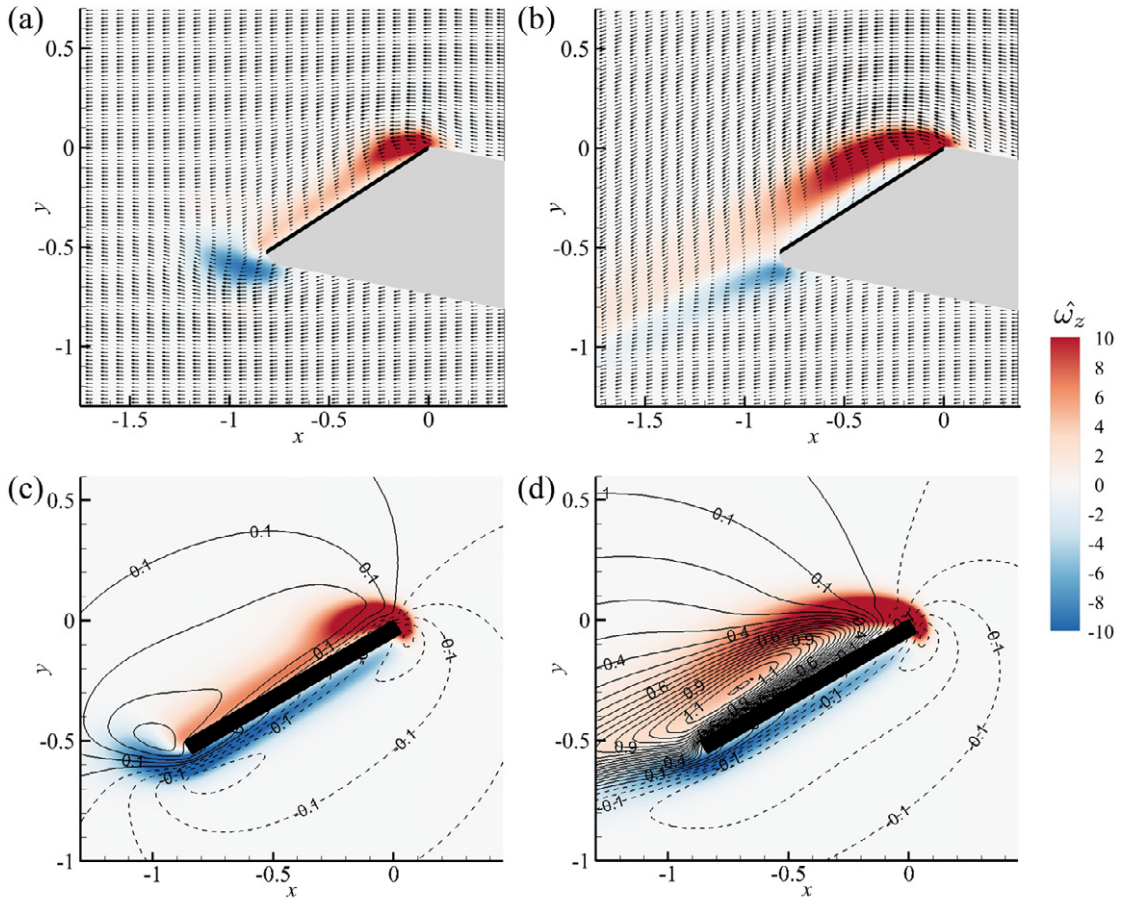


Fig. 4. Representative comparison between the experimental (top row) and numerical (bottom row) results, $Re = 500$ at $z = 0.5$ at two stations during the acceleration phase. The compared quantity is $\hat{\omega}_z$. In-plane vector field is superposed on the experimental results; the numerical results depict contour levels of u_z in addition to $\hat{\omega}_z$ contours. (a,c) $\theta = 10^\circ$; (b,d) $\theta = 90^\circ$.

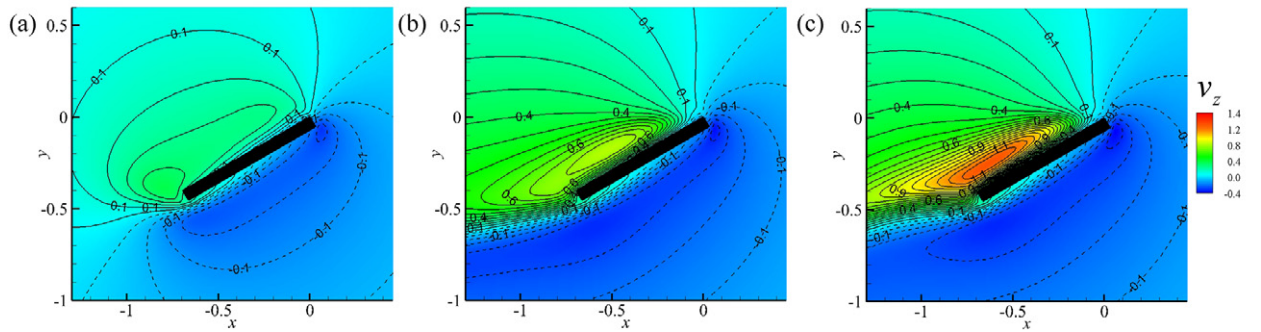


Fig. 5. Evolution of u_z at $Re = 500$, $z=0.4$ during wing acceleration, showing contours and contour levels of the dimensionless spanwise velocity (a) $\theta = 10^\circ$, (b) $\theta = 45^\circ$, (c) $\theta = 90^\circ$.

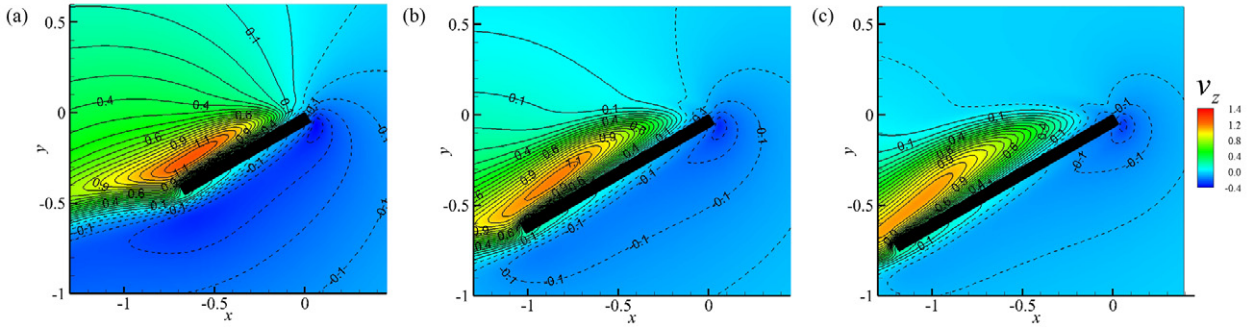


Fig. 6. Distribution of u_z along the wing span at $Re = 500$, $\theta = 90^\circ$ (a) $z=0.4$ (b) $z=0.6$ (c) $z=0.7$.

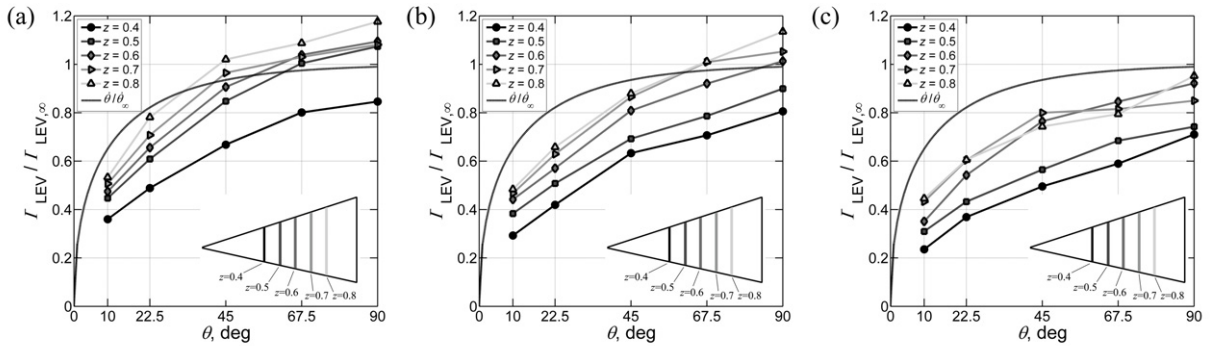


Fig. 7. Evolution of LEV circulation at various span locations (a) $Re = 250$ (b) $Re = 500$ (c) $Re = 1000$. The instantaneous circulation is relative to that evaluated during steady-state wing rotation.

Second, u_z increases monotonically with Reynolds number, enhancing spanwise vorticity convection and inhibiting circulation accumulation along the local chord.

We emphasise that the instantaneous lift coefficient during the acceleration phase is proportional to the product of $\Gamma_{LEV}/\Gamma_{LEV,\infty}$ and $\Gamma_{LEV,\infty}$. As mentioned above, $\Gamma_{LEV}/\Gamma_{LEV,\infty}$ was measured to decrease as Reynolds number increased; however, Γ_{LEV} was almost constant as the Reynolds number changed since $\Gamma_{LEV,\infty}$ increased monotonically with increasing Re in the range $250 < Re < 1000$.

In order to yield an objective comparison between the aerodynamic performance of flapping and rotating wings (at the same Reynolds number) we note that the acceleration phase tested herein is only a partial representation of a realistic flapping wing motion; in a realistic wing motion the wing rotates at both ends of the stroke and starts to accelerate in the opposite direction only after the wing rotation is complete. Previous studies conducted at Reynolds numbers of the order of 100 confirmed that the vorticity production during the wing rotation augmented lift, but in order to arrive at similar conclusions for higher Reynolds numbers, a future study should concentrate on this aspect. Whatever the results of such a study, it is understood that a flapping wing scenario is conceptually different from that of a steady rotating wing: while the flow field over a steady rotating wing should remain steady with an attached LEV to maximise lift, in flapping hovering flight this requirement becomes only secondary since the LEV (or, alternatively, the separation-bubble) should remain on top of the wing surface (and not necessarily stationary) only during half of the stroke compared to the infinite time during which the LEV is required to remain stable in the case of a steady rotating wing. Such a weaker stability restriction provides an advantage of the flapping-wing strategy over rotating wings at increasingly large Reynolds numbers.

4. Conclusions

A combined experimental-numerical study has been undertaken to analyse the vorticity production over an accelerating wing at various Reynolds numbers. The good comparison between the experimental and numerical results allowed use of the spanwise velocity component which was resolved numerically in order to describe the essential flow mechanisms involved. At Reynolds numbers higher than 250 the vorticity was not confined to the vicinity of the leading-edge and remained stable up to a Reynolds number between 1000 and 2000. The evolution of the spanwise velocity component was found to be correlated with the growth of circulation; higher spanwise velocity at larger Reynolds numbers was characterised by slower time evolution of the LEV circulation over the wing.

The results presented here show that at $Re = 250$ the LEV circulation exceeds its steady-state value when the wing approaches the middle of the stroke ($\theta = 90^\circ$). At $Re = 1000$, by contrast, the LEV circulation during the acceleration phase was found to stay considerably below its asymptotic steady wing rotation value. This finding demonstrates that at Reynolds numbers of a few thousand the aerodynamic performance of a flapping wing cannot be well described by a steady rotation analysis which overestimates the actual aerodynamic wing performance.

Most importantly, the results highlight the aerodynamic advantage of flapping flight (over steady wing rotation) at Reynolds numbers above 1000; whereas the LEV becomes unstable during steady wing rotation, the flapping strategy limits the time during which the LEV has to remain stable (or marginally stable) because the LEV is shed by the wing rotation at each end of the half stroke and is then renewed. Each half stroke is thus characterised by a high lift (associated with the LEV) that cannot be attained with steady wing rotation. It is believed that the wing rotation at each end of the half stroke (at $Re > 250$) can produce additional lift and be advantageous to the flapping wing strategy.

Acknowledgements

Y.E. was supported in part by the Joan and Reginald Coleman-Cohen Fund. Numerical simulations were carried out using HPC resources of IDRIS, Paris, project 81664.

References

- [1] Weis-Fogh T. Quick estimates of flight fitness in hovering animals including novel mechanisms for lift production. *The Journal of Experimental Biology*. 1973;59:169–230.
- [2] Van-Den-Berg C, Ellington CP. The three-dimensional leading-edge vortex of ‘hovering’ model hawkmoth. *Phil Trans R Soc Lond B*. 1997;352:329–340.
- [3] Ellington CP, Van-Den-Berg C, Willmott AP, Thomas ALR. Leading-edge vortices in insect flight. *Nature*. 1996;384:626–630.
- [4] Bomphrey RJ, Lawson NJ, Harding NJ, Taylor GK, Thomas ALR. The aerodynamics of *Manduca sexta*: digital particle image velocimetry analysis of the leading-edge vortex. *The Journal of Experimental Biology*. 2005;208:1079–1094.
- [5] Maxworthy T. The formation and maintenance of a leading-edge vortex during the forward motion of an animal wing. *Journal of Fluid Mechanics*. 2007;587:471–475.
- [6] Lentink D, Dickinson MH. Rotational accelerations stabilize leading-edge vortices on revolving fly wings. *The Journal of Experimental Biology*. 2009;212:2705–2719.
- [7] Usherwood JR, Ellington CP. The aerodynamics of revolving wings. II. Propeller force coefficients from mayfly to quail. *The Journal of Experimental Biology*. 2002;205:1547–1564.
- [8] Poelma C, Dickson WB, Dickinson MH. Time-resolved reconstruction of the full velocity field around a dynamically-scaled flapping wing. *Experiments in Fluids*. 2006;41:213–225.
- [9] Dalziel SB. *DigiFlow User Guide*. Dalziel Research Partners; 2003–2009.
- [10] Kolomenskiy D, Moffatt HK, Farge M, Schneider K. Two- and three-dimensional numerical simulations of the clap-fling-sweep of hovering insects. *Journal of Fluids and Structures*. 2011;27(5–6):784–791.
- [11] Angot P, Bruneau CH, Fabrie P. A penalisation method to take into account obstacles in viscous flows. *Numerische Mathematik*. 1999;81:497–520.
- [12] Schneider K. Numerical simulation of the transient behaviour in chemical reactors using a penalisation method. *Method Comput Fluids*. 2005;34:1223–1238.
- [13] Davidson PA. *Turbulence: An introduction for scientists and engineers*. Oxford University Press; 2004.
- [14] Himmelskamp H. Profile investigation on rotating airscrew. Dissertation Gottingen; 1947.